Tunable doublets: piezoelectric glass membrane lenses with an achromatic and spherical aberration control

HITESH G. B. GOWDA,[1] ![ORCID] MATTHIAS C. WAPLER,[1,2] AND ULRIKE WALLRABE[1,*]

[1]*Laboratory for Microactuators, Department of Microsystems Engineering - IMTEK, University of Freiburg, Germany*
[2]*Chair for Microsystems for Medical Engineering, Faculty of Electrical Engineering and Information Technology, Otto von Guericke University Magdeburg, Germany*
[*]*wallrabe@imtek.uni-freiburg.de*

Abstract: We present two versions of tunable achromatic doublets based on each two piezo-electrically actuated glass membranes that create the surface of fluid volumes with different dispersions: a straightforward back-to-back and a more intricate stack of the fluid volumes. In both cases, we can control the chromatic focal shift and focal power independently by a suitable combination of actuation voltages on both active membranes. The doublets have a large aperture of 12 mm at an outer diameter of the actuator of 18 mm, an overall thickness of 3 mm and a short response time of around 0.5 ms and, in addition, provide spherical aberration correction. The two designs have an achromatic focal power range of ±2.2 m^{-1} and ±3.2 m^{-1} or, for the purpose of actively correcting chromatic errors, a chromatic focal shift at vanishing combined focal power of up to ±0.08 m^{-1} and ±0.12 m^{-1}.

1. Introduction

Tunable lenses can enable compact, highly responsive, and simplified systems in imaging applications [1]. They tune their focal power either by refractive index modulation, as in [2–5] or by surface deformation, as in [6–9] to achieve focusing or scanning effect and their applications include, but not limited to, 3D light-sheet microscopy [10–12], two-photon imaging [13–15], confocal microscopy [16–19] and endoscopy [20–22].

However, tunable lenses introduce spherical and chromatic aberrations, which affect the optical quality of the system [23]. On the one hand, these aberrations can be compensated with additional passive optical elements, as in [24]. On the other hand, there exist tunable lenses that allow for spherical aberration correction, either by deforming the optical surface aspherically as in [8,9,25] or by fabricating the optical surface with preset asphericity as in [26]. The former is used to correct sample-induced aspherical aberrations in [17].

Furthermore, tunable lenses with different optical bodies are combined to correct chromatic aberrations in the lens, similar to traditional doublets [27]. The tunable chromatic lenses or doublets in [28–32] include 2 to 6 deformable surfaces, resulting in different fluid volumes. The doublets in [28–31] are based on the electro-wetting actuation principle, which requires fluids not only with suitable optical properties but also a non-miscible combination with insulating or conductive properties, e.g., oils vs. water-based solutions. Additionally, the slow response time, in the range of 10 ms to 100 ms, and the high sensitivity of liquids to mechanical shocks, limit the electro-wetting lenses [1]. Furthermore, the lenses in [29,30] address only either spherical or chromatic aberration.

We propose an alternative approach to address both the spherical and chromatic aberration correction in a single component by combining two highly responsive active piezo-glass-piezo

sandwich membranes [8,9] with two fluid chambers that are filled with optical oils of different refractive indices and Abbe numbers.

In this paper, we introduce two possible layouts: a back-to-back design where the fluid chambers are separated by a rigid glass window and have the active membranes towards the outside, and a stack design, where the separating interface and one outer interface are made from active membranes. We describe their design and analytical model in section 2, and the fabrication and fluid selection in section 3. In section 4, we present the opto-mechanical characterization of the tunable achromats with a quasi-static response, chromatic aberration computed at different curvature ratios over a visible wavelength spectrum, Zemax simulation model, dynamic response and conclude the paper in section 5.

2. Mechanical designs of the tunable doublets

The doublets are based on the singlet [8,9], which consists of an active optical membrane, where an ultra-thin glass membrane is sandwiched between two piezo ceramic rings. This active membrane is mounted on an elastic chamber filled with an optical fluid. A combination of electric fields can be applied to the piezos to achieve two operating modes: a bending mode and a buckling mode. In the former, one piezo expands, and the other contracts to produce a bending moment, which deforms the membrane with a rather spherical or elliptical profile, as in Fig. 1(a). The curvature (R^{-1}_{bending}) is then proportional to the transverse piezoelectric coefficient (d_{31}), the difference of the applied electric fields (E_1, E_2), the refractive index (n), and approximately inversely proportional to the combined thickness (t) of the glass membrane, intermediate glue, and one other piezo layer:

$$R^{-1}_{\text{bending}} \propto d_{31} (E_1 - E_2)/t. \tag{1}$$
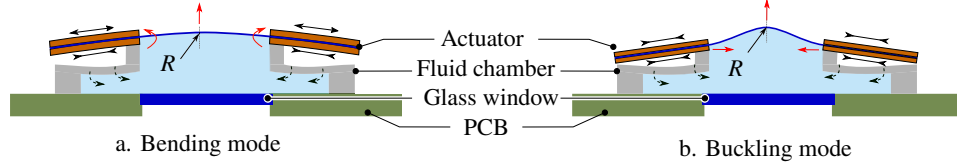
Fig. 1. Schematic cross section of the singlet lens showing deformed active membrane in (a.) bending mode and (b.) buckling mode.

In the buckling mode, both piezos contract radially to buckle the membrane, which leads to a rather hyperbolical surface profile, as in Fig. 1(b). The curvature (R^{-1}_{buckling}) is non-linear, i.e., proportional to the square root of the electric fields and piezoelectric coefficient, and the length scale of the curvature is given by the membrane diameter (D_{m}):

$$R^{-1}_{\text{buckling}} \propto D_{\text{m}}^{-1} \sqrt{d_{31} (E_1 + E_2)}. \tag{2}$$

Combining the bending and buckling modes then allows to tune the curvature (R^{-1}) and the spherical aberration simultaneously by essentially giving the glass membrane tunable Dirichlet and von Neumann boundary conditions [8,9,25].

Rather than a single membrane with a single fluid for refraction, we now use two membranes with two fluid chambers filled with optical fluids of different dispersions to address also the chromatic aberration, similar to the crown and the flint glasses in classical achromatic lenses. The simpler approach with a more straight forward fabrication is to essentially combine these lenses back-to-back. A more sophisticated approach is to stack them such that one membrane serves as an interface between both fluids and the other one as an outer interface.
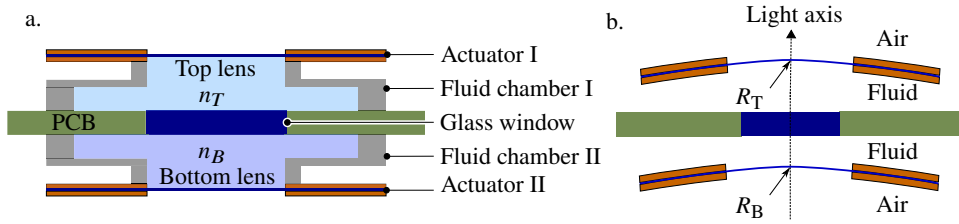
2.1. Back-to-back design

Figure 2(a) shows the schematic cross-section of the back-to-back design of the doublet. Both membranes in the doublet can be actuated independently. An example actuation scenario is shown in Fig. 2(b). The top fluid chamber is filled with a fluid with a high Abbe number (ν_T). In contrast, the bottom volume is filled with a fluid with a low Abbe number (ν_B). In the approximation of a thin lens, the combined focal power ($f_{\lambda_n}^{-1}$) of the doublet at a wavelength (λ_n) is the summation of the individual focal powers resulting from the top (f_T^{-1}) and bottom (f_B^{-1}) membranes:

$$f_{\lambda_n}^{-1} \approx f_T^{-1} + f_B^{-1} . \tag{3}$$

Further, the combined focal power can then be written by the Lens-maker's formula as a function of the refractive indices $n_T^{\lambda_n}$ and $n_B^{\lambda_n}$ of the fluids and the curvatures of the membranes R_T^{-1} and R_B^{-1}, and is given by

$$f_{\lambda_n}^{-1} \approx (n_T^{\lambda_n} - 1)R_T^{-1} - (n_B^{\lambda_n} - 1)R_B^{-1}, \tag{4}$$

with a '+' sign convention for the curvatures with the surface bending upwards. The subscripts T and B represent the top and bottom lenses.

Fig. 2. Back-to-back design of the piezoelectric doublet lens showing (a.) the schematic cross section and (b.) the working schematic at the example of the membranes deformed with the bending actuation.

Achromatic lenses correct the focal power at two different wavelengths (λ_1 and λ_2), which means that both membranes are actuated proportionally in the same directions, such that the dispersion of both fluids cancels. Further, equating $f_{\lambda_1}^{-1} = f_{\lambda_2}^{-1}$ gives us the ratio of the curvatures

$$\frac{R_T^{-1}}{R_B^{-1}} = \frac{n_B^{\lambda_2} - n_B^{\lambda_1}}{n_T^{\lambda_2} - n_T^{\lambda_1}} = \frac{\Delta n_B}{\Delta n_T}, \tag{5}$$

in terms of the refractive indices of the fluids in top and bottom chamber at wavelengths λ_1 and λ_2, $n_T^{\lambda_2}$, $n_T^{\lambda_1}$, $n_B^{\lambda_2}$ and $n_B^{\lambda_1}$. The achromatic focal power is then given by

$$f_{\lambda_1}^{-1} \approx \left((n_T^{\lambda_1} - 1) - (n_B^{\lambda_1} - 1) \frac{\Delta n_T}{\Delta n_B} \right) R_T^{-1} . \tag{6}$$

We notice that the ratio of curvatures $\frac{R_T^{-1}}{R_B^{-1}}$ is always positive, so we have always one convex and one concave outer surface, as we expect from the textbook achromatic condition [33] given by

$$\frac{1}{f_T \nu_T} + \frac{1}{f_B \nu_B} = 0 . \tag{7}$$

2.2. Stack design

Figure 3(a) shows the schematic cross-section of the stack design of the doublet. The top and bottom fluid volumes are filled with fluids identical to the previous design. Again, the membranes can be actuated independently with an example actuation shown in Fig. 3(b). The combined focal power ($f_{\lambda_n}^{-1}$) given by Eq. (6) becomes in this configuration

$$f_{\lambda_n}^{-1} \approx (n_T^{\lambda_n} - 1)R_T^{-1} - (n_T^{\lambda_n} - n_B^{\lambda_n})R_B^{-1},$$ (8)

and with the same sign convention, + for surface bending upwards, the ratio of the curvatures for the achromatic configuration becomes

$$\frac{R_T^{-1}}{R_B^{-1}} = 1 - \frac{n_B^{\lambda_2} - n_B^{\lambda_1}}{n_T^{\lambda_2} - n_T^{\lambda_1}} = \frac{\Delta n_T - \Delta n_B}{\Delta n_T} \ .$$ (9)
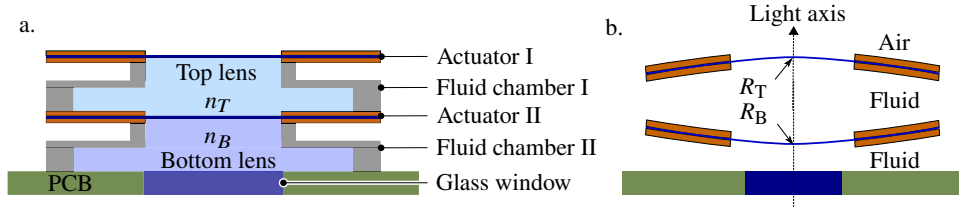
Fig. 3. Stack design of the piezoelectric doublet lens showing (a.) the schematic cross section and (b.) the working schematic at the example of deformed membranes.

The achromatic focal power is similarly given by

$$f_{\lambda_1}^{-1} = \left((n_T^{\lambda_1} - 1) - (n_T^{\lambda_1} - n_B^{\lambda_1}) \left(\frac{\Delta n_T}{\Delta n_T - \Delta n_B} \right) \right) R_T^{-1} \ .$$ (10)

Now, the ratio $\frac{R_T^{-1}}{R_B^{-1}}$ is negative since $n_T < n_B$ and this results in the stack configuration in a bi-convex (or concave) upper volume and a plano-concave (or convex) lower volume as expected.

3. Fabrication

We used a nanosecond UV laser to structure the $100\,\mu m$ thick piezo ceramic rings from Johnson Matthey ($M1100$) [34], $50\,\mu m$ thick glass membranes and $500\,\mu m$ thick glass substrate from SCHOTT ($D263t$ eco) [35], and a $500\,\mu m$ thick PCB (FR-4) substrate. To form the active membranes, we glued piezo rings on both sides of the glass membrane. We then cast the polyurethane fluid chambers from Smooth-On (ClearFlex 50) [36], and glued to the active membranes and the glass window into the 12 mm hole in the PCB. For the back-to-back design, we glued two such active elements concentrically on both sides of the PCB. Finally, we filled two different fluids in the two chambers with the help of a pressurized fluid dispenser and a vacuum arrangement. In the stack design, we first completed the bottom fluid volume on the PCB, by gluing the active membrane on the PCB and filling fluid in the chamber, and similarly completed the top fluid volume.

Now considering the optical fluid selection, the traditional achromatic doublets are made from crown glass that has low dispersion (high Abbe number) and flint glass showing high dispersion (low Abbe number) [28]. For our lens, we are limited to non-polar fluids due to the chemical compatibility of the fluid chamber, and hence there are the options of hydrocarbons with a

higher refractive index and strong dispersion, and halocarbons with a lower refractive index and weak dispersion, in particular fluorocarbons. In Fig. 4(a), we show the refractive index as a function of the wavelength for a selection of hydrocarbons and in Fig. 4(b) for halocarbons. We compare these fluids with the standard glass types in the Abbe diagram in Fig. 4(c). We chose perfluorodecalin with an Abbe number of $V_d = 114$ for the low dispersion in the top volume and paraffin with an Abbe number of $V_d = 56$ for the high dispersion in the bottom chamber.
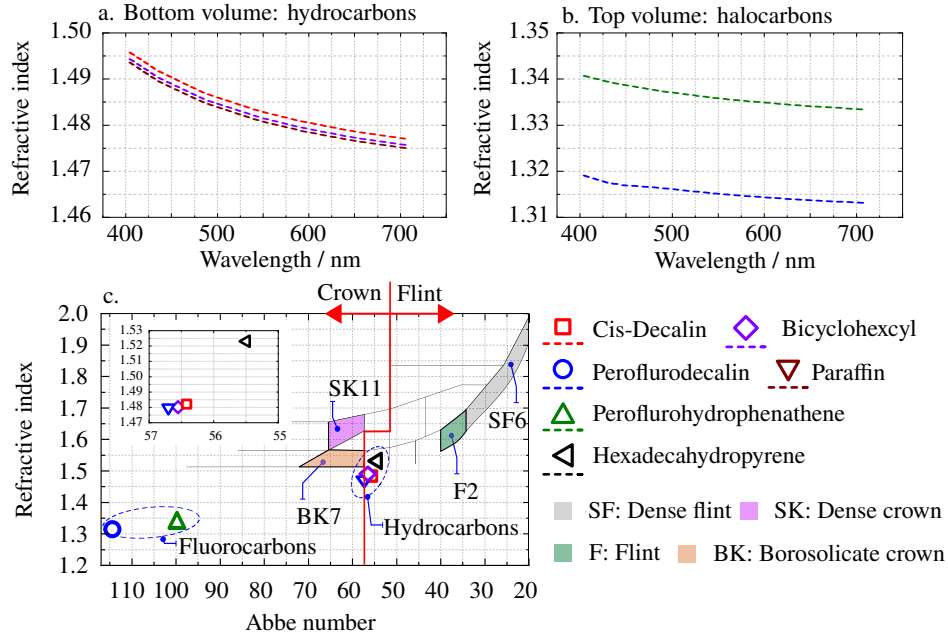
Fig. 4. (a.) Dispersion behavior of the optical fluids with hydrocarbons-C_nH_{2n} and (b.) halo carbons (flurocarbons) - C_nF_m. (c.) Abbe diagrams of the optical fluids and some common glasses [37].

4. Opto-mechanical characterization

As the focal power of the doublet directly depends on the curvature of the deformed membranes and the refractive index of the fluids (Eq. (6) and 10) and in contrast, the effects from the thin glass membranes themselves are expected to be negligible, we measured the membrane deformation with a distance sensor to scan the surface point-wise with a translational stage while applying a slow periodic signal of 1 Hz with a signal generator and a voltage amplifier. In [9], we estimated the optical path difference due to the membrane to around 1 nm in a similar setup. We used a confocal distance sensor with a resolution of 17 nm for quasi-static measurements and a high sampling rate triangulation sensor with a resolution of 20 nm for unit step response measurements.

4.1. Quasi-static response

We limited the applied electric field on the piezos to $1.5\,\text{kV}\,\text{mm}^{-1}$ in the direction of the polarization to avoid electrostatic breakdown and to $-0.4\,\text{kV}\,\text{mm}^{-1}$ against the direction of polarization to avoid depolarization. For the bending mode, we applied symmetric electric fields with a phase shift of $180°$ on the two piezos of the actuator and for the buckling mode, without the phase shift, as in Fig. 5(a) and (b) and additionally, a sequential mode, as in Fig. 5(c), to actuate a

combination of the bending and buckling modes that outlines the overall stable operating range of the membranes.

We fit the measured membrane profile (x,y,z) with an fourth order aspherical function given by

$$z(x, y) = \alpha_0 + \alpha_x + \alpha_y + \alpha_2(x^2 + y^2) + \alpha_4(x^2 + y^2)^4, \tag{11}$$

and determined the curvature $R^{-1} \approx 2\alpha_2$ and the spherical aberration Zernike coefficient $Z_4^0 = (r^4\alpha_4)/6$, where r is the radius of aperture. We observe the typical hysteresis of the piezo material in the curvatures defined as a function of the applied electric field in bending and buckling modes, shown in Fig. 6(a)–(d). The pure bending mode results in a symmetric, though only small focal power range compared to the buckling mode, which is highly non-linear and does not actively control the direction.
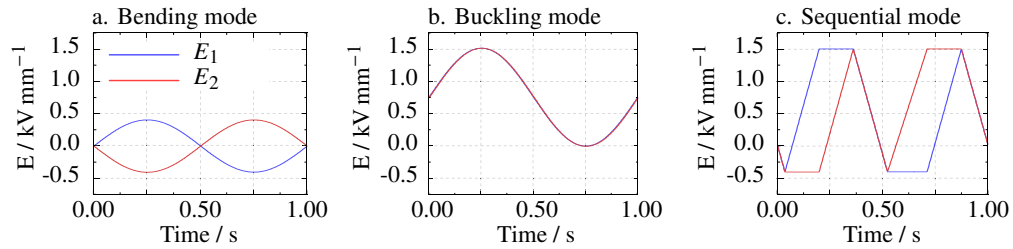
Fig. 5. Electric fields (E_1 and E_2) applied to the two piezos of the actuator in bending mode (a.), buckling mode (b.) and sequential mode (c.).

We can control this direction, however, in the sequential actuation mode, shown in Fig. 6(e) and (f), where we see that all the membranes can be deformed independently to achieve a tunable curvature range of around ±13.5 m^{-1}. Additionally, we see that with our particular geometry, the surface is almost parabolic in the bending mode and becomes hyperbolic as soon as we add buckling, which corresponds to a spherical aberration correction range of approximately ±2 μm.

For the stack design, we characterized also the cross-talk between the membranes by measuring a passive membrane while the other one was actuated, as both membranes share the same fluid volume, so they may interact through the pressure in the fluid. In Fig. 7, we see that this is very small with around ±0.01 m^{-1} or 2% of the maximum tuning range in bending mode and approx. ±0.03 m^{-1} or 0.5% in the buckling mode.

4.2. Ray tracing model

To verify, that the mechanical characterization with the analytical approximation equations (Eq. (6) and Eq. (10)) give us indeed good values for the focal power and chromatic shift, we also developed a ray tracing model in Zemax as shown in Fig. 8(a), by considering the optical fluids as glass materials with an appropriate third order Sellmeier fit. For simplicity, we have considered a spherical curvature of the membrane in the simulation, which is sufficient for comparing the focal powers and their required curvature ratios in order to study the effects of the lens and membrane thicknesses. Figure 8(b) shows the resulting spot diagram at the example of a stack doublet at 3.2 m^{-1} at zero chromatic focal shift and at an induced maximum chromatic focal shift at same focal power, and a close-up of the ray tracing near the foci. We can clearly see the effect of the achromatic focusing and the chromatic confocal shift, respectively.

4.3. Chromatic aberration

From the quasi-static response, we computed the combined focal power and the chromatic focal shift for the standard wavelength pair $\lambda_1 = 486$ nm and $\lambda_2 = 589$ nm (Sodium F and D lines).
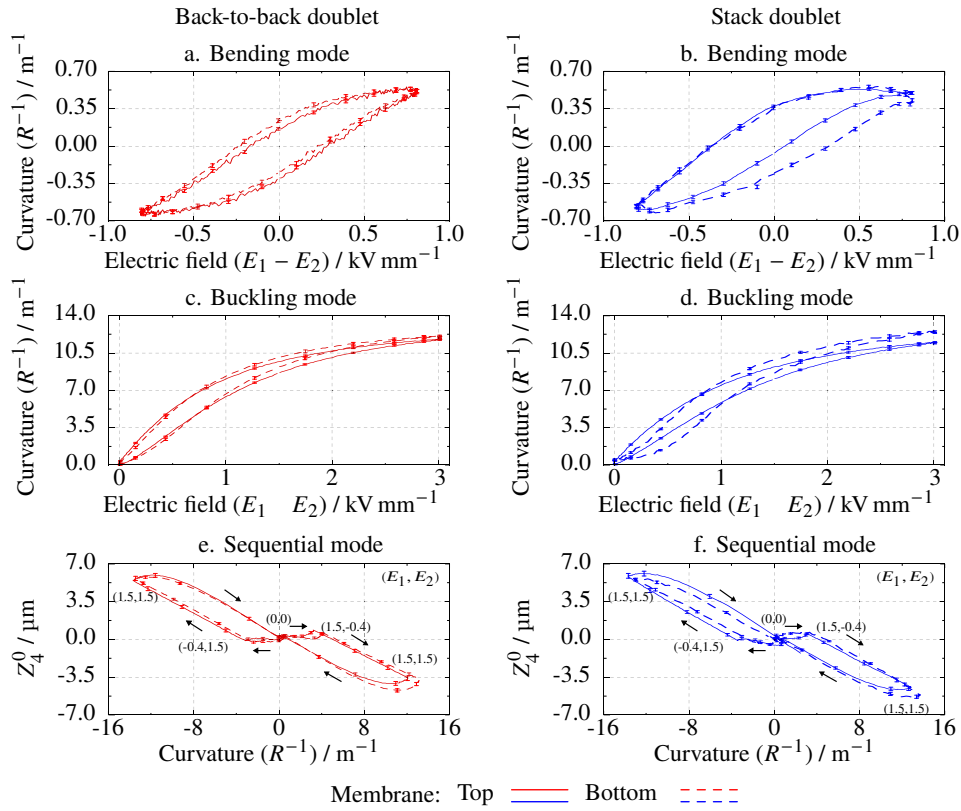
Fig. 6. The curvatures of the membranes of the back-to-back (a,c) and stack doublet (b,d) actuated in bending and buckling mode. The working range in terms of curvature (R^{-1}) and spherical aberration Zernike coefficient (Z_4^0) from the sequential mode of the back-to-back (e) and stack doublet (f).
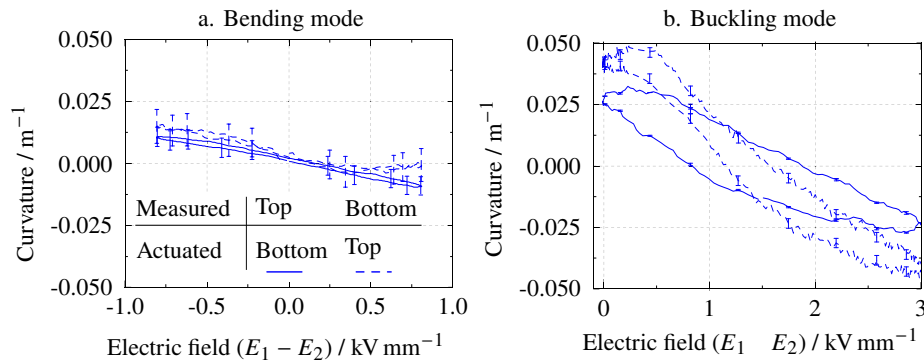

Fig. 7. Cross-talk between the optical surfaces of the stack design with one membrane active and one passive in (a.) bending mode and (b.) buckling mode. The error bars denote the standard deviation from 3 measurement cycles.

a. Doublet layouts (achromatic condition)

b. Spot and ray diagram
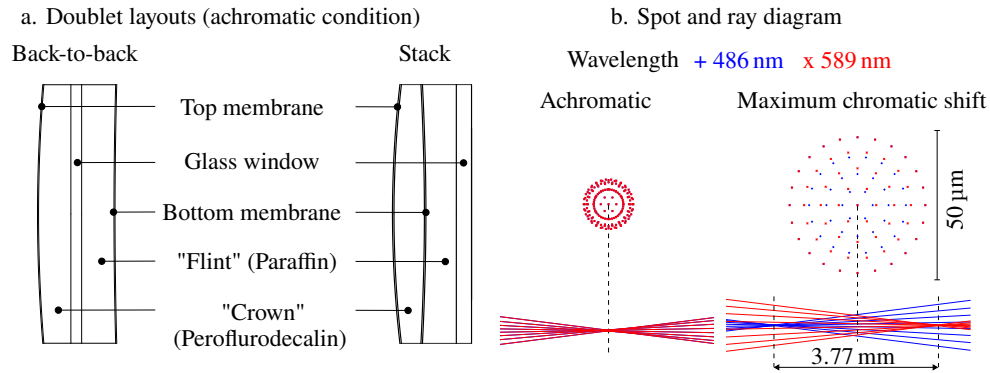
Fig. 8. (a.) Zemax layout of the back-to-back and stack doublet in an achromatic configuration at 2.2 m^{-1} and 3.2 m^{-1}. The two surfaces of the membranes (50 μm may not be clearly visible in the layout. (b.) Spot diagram and ray diagram (radial axis scaled by 10) of stack at a focal power of 3.2 m^{-1} in the achromatic condition and at maximum chromatic focal shift for a wavelength pair of 486 nm and 589 nm.

To look at how the two curvatures affect the behavior of the lens, we show the range of the focal power in Fig. 9(a) (back to back) and Fig. 9(b) (stacked) as a function of the ratio of curvatures. The solid lines show the focal power whenever the greater one of both curvatures is ± 13.5 m^{-1} and the other one is adjusted according to the ratio $\frac{R_T^{-1}}{R_B^{-1}}$. The dashed lines show the corresponding focal power shift. In particular, we show the variation in focal power as $\Delta\left(f^{-1}\right)$ rather than the change in focal length, as Δf would obviously diverge then f^{-1} is zero (i.e., f is infinite).
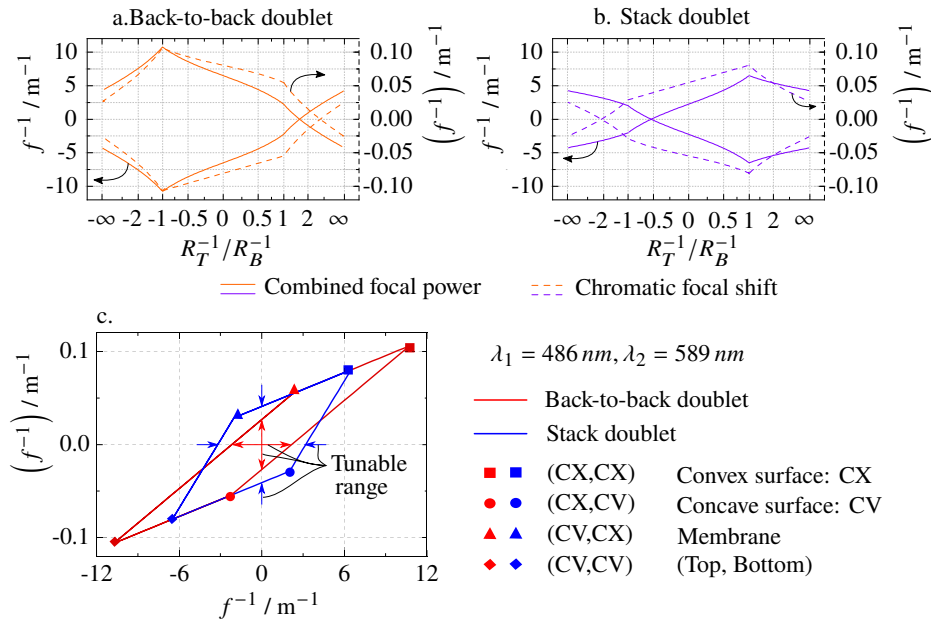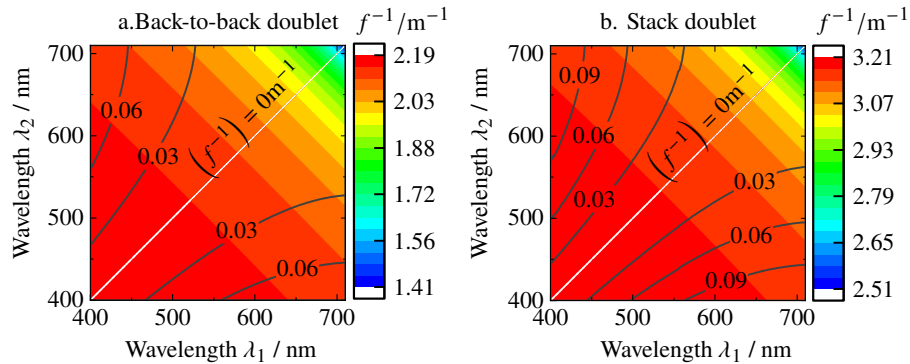

Fig. 9. Combined focal power (f^{-1}) and chromatic focal shift ($\Delta(f^{-1})$) as a function of the curvature ratios (R_T^{-1}/R_B^{-1}) at $\lambda_1 = 486$ nm and $\lambda_2 = 589$ nm with the back-to-back doublet (a.) and stack doublet (b.); Comparison of tunable combined focal power and chromatic focal shift (c.).

We find that for the back-to-back layout, the focal power and focal shift are closely related whenever the curvatures are opposite, as then we essentially have a biconvex or biconcave lens. At curvatures in the same direction i.e., forming meniscus lenses, we see the actual chromatic effects, where we can tune the focal power independently from the chromatic shift (i.e., achromaticaly) at a ratio $\frac{R_T^{-1}}{R_B^{-1}} = 3.07$ and we can tune the chromatic shift at vanishing focal power at $\frac{R_T^{-1}}{R_B^{-1}} = 1.48$. For the stacked design, the simple lens occurs at curvatures in the same direction, but already there we see that the ratio of curvatures has a much greater effect on the ratio between the focal power and chromatic shift. The effects of achromatic focusing and chromatic shifting occur at $\frac{R_T^{-1}}{R_B^{-1}} = -2.14$ and $\frac{R_T^{-1}}{R_B^{-1}} = -0.5$ and are much more pronounced than in the back to back design. This is because viewed from the outside, we have just a plano-convex or plano-concave lens with an additional deformable interface between the two materials.

This fundamental difference between both designs can also be seen when we look at the tuning range of the lenses. Fig. 9(c) compares the outline of the achievable range of the chromatic focal shift and combined focal power for the two versions of the doublets. We see that the back-to-back configuration has a highest overall maximum focal power of ±10.8 m^{-1} compared to ±6.5 m^{-1} for the stacked configuration. However, the stacked configuration has a better control over the chromatic focal shift, resulting in a maximum achromatic focal power of ±3.21 m^{-1} and a tuning range of the chromatic focal shift at vanishing net focal power of ±0.041 m^{-1}, compared to ±2.21 m^{-1} and ±0.026 m^{-1} in the back-to-back configuration.

Figure 10 shows the range of the achromatic focal power (colors) and maximum chromatic focal shift (contour lines) as a function of the two wavelengths over the full visible wavelength spectrum from 400 nm to 700 nm. As expected, we have the strongest chromatic shift for highly different wavelengths. The achromatic focusing range, is on the one hand, dominated by the overall refractive index and, on the other hand, by the ratio of the fluid dispersions. For instance with the back-to-back doublet, at $\lambda_1 = 400$ nm and $\lambda_2 = 500$ nm, the dispersion ratio (Eq. (5)) is around 0.5, which is more compared to around 0.4 at $\lambda_1 = 400$ nm and $\lambda_2 = 700$ nm, hence the focusing range is higher for smaller overall wavelengths.

Fig. 10. Induced chromatic focal shift ($\Delta(f^{-1})$) and the combined focal power (f^{-1}) over the visible light wavelength range of $\lambda_1 = 400$ nm to $\lambda_2 = 700$ nm. Contour lines denote the chromatic focal shift at vanishing focal powers and contour colors denote the achromatic focal power.

The back-to-back doublet, as in Fig. 10(a), has a maximum achromatic focal power between 1.4 m^{-1} and 2.2 m^{-1}, shown as contour colors, depending on the wavelength pair. The maximum chromatic focal shift at vanishing combined focal power varies from 0 m^{-1} to 0.08 m^{-1}. Similarly, the stacked doublet, as in Fig. 10(b), has a maximum achromatic focal power range between 2.5 m^{-1} and 3.2 m^{-1} and the maximum chromatic focal shift at vanishing combined focal power

— Analytical   — Zemax   — Standard achromat (Thorlabs AC254-300-A)
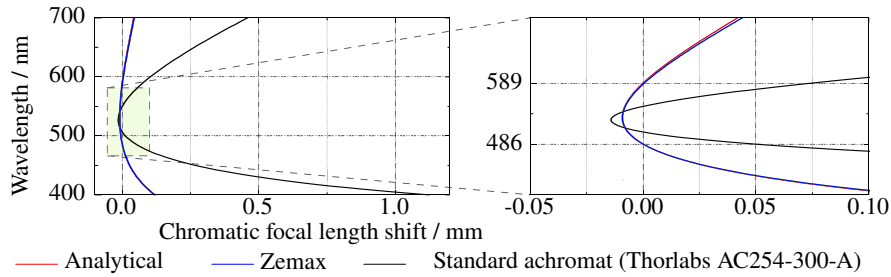
Fig. 11. Achromatic behavior of a classical glass achromatic lens with fixed focal power of $3.3\ \mathrm{m}^{-1}$ [38] and stack doublet computed with analytical model and with Zemax model at $3.2\ \mathrm{m}^{-1}$.

varies from $0\ \mathrm{m}^{-1}$ and $0.12\ \mathrm{m}^{-1}$. Overall, we see that over most of the wavelengths, we have a focusing range near the maximum value.

Comparing the results quantitatively, we see almost identical results, with $R_\mathrm{T} = 13.50\ \mathrm{m}^{-1}$ $R_\mathrm{B} = 6.35\ \mathrm{m}^{-1}$ in the analytical estimate at $3.2\ \mathrm{m}^{-1}$ achromatic focusing and $R_\mathrm{T} = 13.51\ \mathrm{m}^{-1}$ $R_\mathrm{B} = 6.31\ \mathrm{m}^{-1}$ as the result from the Zemax model, both for the stacked doublet. The results for the back-to-back design show a similar deviation. In particular, we see no measurable difference when comparing a simulation with and without the ultra-thin membrane ($50\,\mu$ m). This also demonstrates that our surface characterization gives reliable results for the optical properties.

Finally, let us compare the achromatic behavior of our lens to classical rigid achromatic lenses made from glass. In Fig. 11, we show the usual plot of the chromatic focal length shift for a standard N-BK7/N-SF2 lens with focal power of $3.3\ \mathrm{m}^{-1}$ [38] and compare it to our stack lens when operated at the maximum focal power of $3.2\ \mathrm{m}^{-1}$. We see a much smaller remaining chromatic focal shift compared to the glass lens because of the properties of the optical materials.
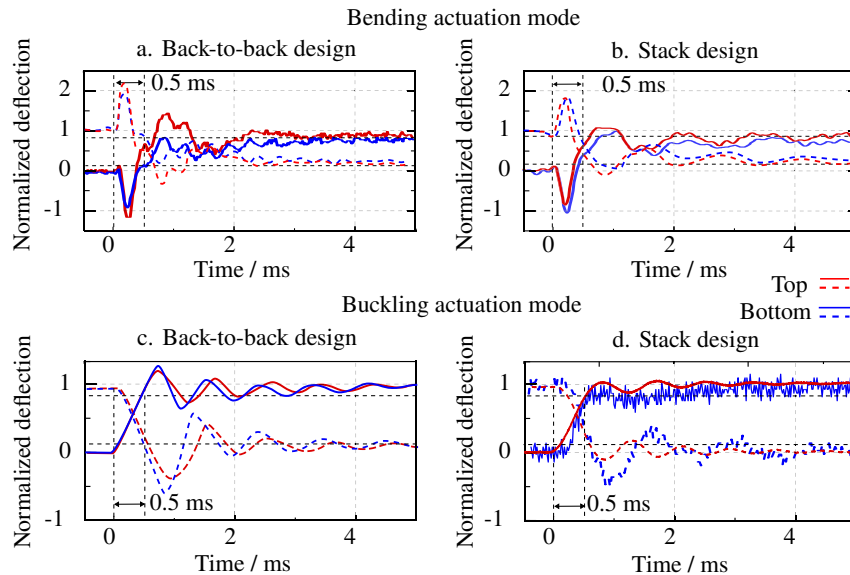
Fig. 12. Dynamic behavior of the doublets with the step response in bending (a. and b.) and buckling actuation modes (c. and d.).

The back-to-back and stack lens would be the same at the same focal power. Also here, we see only a very small deviation between the analytical estimate and the ray tracing simulation.

4.4. Dynamic response

To measure the step response, we actuated each membrane individually with a step function ± 0.4 kV mm^{-1} in the electric field in bending mode and 1 kV mm^{-1} in buckling mode at 1 Hz and measured the displacement at the center of the membrane. The 90% rise and 10% fall time are around 0.5 ms in all cases, as in Fig. 12, followed by a settling behavior that lasts few milliseconds. This could further be reduced either by a closed-loop control or a smoother driving signal that reduces the excitation of this resonance.

5. Summary

We have presented tunable doublets based on piezo-glass-piezo active sandwich membranes [8]. We combined two membranes with two fluid chambers filled with different fluids (hydrocarbons and halocarbons) to realize a simple back-to-back combination with the active membranes at the outer interfaces, and a more intricate stack combination with one active membrane outside and one in between two fluids. The doublets have an aperture of 12 mm at a small footprint of 18 mm as defined by the actuators, and a thickness of only 3 mm. The response time of the doublets is approximately 0.5 ms in all configurations. The two lenses can be actuated independently to control the curvature ratio of the membranes and achieve the required chromatic shift. After measuring the electric response of the surface profiles of the lenses in different actuation modes, we found that the maximum combined focal power range was around ± 11 m^{-1} for the back-to-back design and was around ± 6.5 m^{-1} for the stack design. The achromatic tuning ranges are, however, ± 2.2 m^{-1} and ± 3.2 m^{-1} and similarly the maximum induced chromatic focal shift at vanishing net focal power are ± 0.08 m^{-1} and ± 0.12 m^{-1}, respectively. This implies that overall the stacked design has a better control over the chromatic behavior because of the bi-curvature lens at the top volume as compared to the single curvature lens in the back-to-back design. These values compare to a focusing range of ± 6 m^{-1} of a singlet lens with only one membrane active. The aspherical behavior used for spherical aberration correction is inherited from the singlet lenses [8,9,25]. With the two membranes, there is, in principle the possibility to correct also the chromatic shift in the aspherical coefficient. Additionally, using different geometries for both the membranes, there may be the possibility to correct also second order spherical aberration, obviously at the cost of a further reduced focusing range. Finally, the underlying analytical estimates agree extremely well with the Zemax simulation model, which, in turn, also demonstrates that our purely mechanical characterization can reliably predict the optical properties.

Disclosures. The authors declare no conflicts of interest.

Data availability. Data underlying the results presented in this paper are not publicly available at this time but may be obtained from the authors upon reasonable request.

References

1. L. Chen, M. Ghilardi, J. J. Busfield, and F. Carpi, "Electrically tunable lenses: a review," Front. Robot. AI **8**, 1 (2021).
2. K. A. Higginson, M. A. Costolo, E. A. Rietman, J. M. Ritter, and B. Lipkens, "Tunable optics derived from nonlinear acoustic effects," J. Appl. Phys. **95**(10), 5896–5904 (2004).
3. D.-K. Yang and S.-T. Wu, *Fundamentals of liquid crystal devices* (John Wiley & Sons, 2014).
4. S. Sato, "Liquid-crystal lens-cells with variable focal length," Jpn. J. Appl. Phys. **18**(9), 1679–1684 (1979).
5. Y.-H. Lin, Y.-J. Wang, and V. Reshetnyak, "Liquid crystal lenses with tunable focal length," Liq. Cryst. Rev. **5**(2), 111–143 (2017).

6. J. Draheim, F. Schneider, R. Kamberger, C. Mueller, and U. Wallrabe, "Fabrication of a fluidic membrane lens system," J. Micromech. Microeng. **19**(9), 095013 (2009).

7. B. Hendriks, S. Kuiper, M. V. As, C. Renders, and T. Tukker, "Electrowetting-based variable-focus lens for miniature systems," Opt. Rev. **12**(3), 255–259 (2005).

8. M. C. Wapler, M. Stürmer, and U. Wallrabe, "A compact, large-aperture tunable lens with adaptive spherical correction," in *2014 International Symposium on Optomechatronic Technologies*, (IEEE, 2014), pp. 130–133.

9. M. C. Wapler, "Ultra-fast, high-quality and highly compact varifocal lens with spherical aberration correction and low power consumption," Opt. Express **28**(4), 4973–4987 (2020).

10. F. O. Fahrbach, F. F. Voigt, B. Schmid, F. Helmchen, and J. Huisken, "Rapid 3d light-sheet microscopy with a tunable lens," Opt. Express **21**(18), 21010–21026 (2013).

11. P. N. Hedde and E. Gratton, "Selective plane illumination microscopy with a light sheet of uniform thickness formed by an electrically tunable lens," Microsc. Res. Tech. **81**(9), 924–928 (2018).

12. S. Bakas, D. Uttamchandani, H. Toshiyoshi, and R. Bauer, "Mems enabled miniaturized light-sheet microscopy with all optical control," Sci. Rep. **11**(1), 14100 (2021).

13. B. F. Grewe, F. F. Voigt, M. van 't Hoff, and F. Helmchen, "Fast two-layer two-photon imaging of neuronal cell populations using an electrically tunable lens," Biomed. Opt. Express **2**(7), 2035–2046 (2011).

14. J. L. Chen, O. A. Pfäffli, F. F. Voigt, D. J. Margolis, and F. Helmchen, "Online correction of licking-induced brain motion during two-photon imaging with a tunable lens," The J. physiology **591**(19), 4689–4698 (2013).

15. N. Olivier, A. Mermillod-Blondin, C. B. Arnold, and E. Beaurepaire, "Two-photon microscopy with simultaneous standard and extended depth of field using a tunable acoustic gradient-index lens," Opt. Lett. **34**(11), 1684–1686 (2009).

16. J. M. Jabbour, B. H. Malik, C. Olsovsky, R. Cuenca, S. Cheng, J. A. Jo, Y.-S. L. Cheng, J. M. Wright, and K. C. Maitland, "Optical axial scanning in confocal microscopy using an electrically tunable lens," Biomed. Opt. Express **5**(2), 645–652 (2014).

17. K. Philipp, A. Smolarski, N. Koukourakis, A. Fischer, M. Stürmer, U. Wallrabe, and J. W. Czarske, "Volumetric hilo microscopy employing an electrically tunable lens," Opt. Express **24**(13), 15029–15041 (2016).

18. K. D. Mac, M. M. Qureshi, M. Na, S. Chang, T. J. Eom, H. S. Je, Y. R. Kim, H.-S. Kwon, and E. Chung, "Fast volumetric imaging with line-scan confocal microscopy by electrically tunable lens at resonant frequency," Opt. Express **30**(11), 19152–19164 (2022).

19. N. Koukourakis, M. Finkeldey, M. Stürmer, C. Leithold, N. C. Gerhardt, M. R. Hofmann, U. Wallrabe, J. W. Czarske, and A. Fischer, "Axial scanning in confocal microscopy employing adaptive lenses (cal)," Opt. Express **22**(5), 6025–6039 (2014).

20. Y. Zou, W. Zhang, F. S. Chau, and G. Zhou, "Miniature adjustable-focus endoscope with a solid electrically tunable lens," Opt. Express **23**(16), 20582–20592 (2015).

21. P. Zhao, Ç. Ataman, and H. Zappe, "An endoscopic microscope with liquid-tunable aspheric lenses for continuous zoom capability," in *Micro-Optics 2014*, vol. 9130 (SPIE, 2014), pp. 17–27.

22. M. E. Pawlowski, S. Shrestha, J. Park, B. E. Applegate, J. S. Oghalai, and T. S. Tkaczyk, "Miniature, minimally invasive, tunable endoscope for investigation of the middle ear," Biomed. Opt. Express **6**(6), 2246–2257 (2015).

23. Y. Yan, X. Tian, R. Liang, and J. Sasian, "Optical performance evaluation and chromatic aberration correction of a focus tunable lens used for 3d microscopy," Biomed. Opt. Express **10**(12), 6029–6042 (2019).

24. J. A. Strother, "Reduction of spherical and chromatic aberration in axial-scanning optical systems with tunable lenses," Biomed. Opt. Express **12**(6), 3530–3552 (2021).

25. F. Lemke, Y. Frey, B. P. Bruno, K. Philipp, N. Koukourakis, J. Czarske, U. Wallrabe, and M. C. Wapler, "Multiphysics simulation of the aspherical deformation of piezo-glass membrane lenses including hysteresis, fabrication and nonlinear effects," Smart Mater. Struct. **28**(5), 055024 (2019).

26. P. Zhao, Ç. Ataman, and H. Zappe, "Spherical aberration free liquid-filled tunable lens with variable thickness membrane," Opt. Express **23**(16), 21264–21278 (2015).

27. E. Hecht, *Optics 4th edition by Eugene Hecht Reading* (Addison-Wesley Publishing Company, MA, 2001).

28. S. Reichelt and H. Zappe, "Design of spherically corrected, achromatic variable-focus liquid lenses," Opt. Express **15**(21), 14146–14154 (2007).

29. L. Wang, H. Oku, and M. Ishikawa, "An adaptive achromatic doublet design by double variable focus lenses," in *Novel Optical Systems Design and Optimization XVII*, vol. 9193 (International Society for Optics and Photonics, 2014), p. 91930O.

30. L. Li and Q.-H. Wang, "Zoom lens design using liquid lenses for achromatic and spherical aberration corrected target," Opt. Eng. **51**(4), 043001 (2012).

31. J.-H. Wang, W.-P. Tang, L.-Y. Li, L. Xiao, X. Zhou, and Q.-H. Wang, "Hybrid driving variable-focus optofluidic lens," Opt. Express **27**(24), 35203–35215 (2019).

32. P. Rajaeipour, K. Banerjee, A. Dorn, H. Zappe, and Ç. Ataman, "Cascading optofluidic phase modulators for performance enhancement in refractive adaptive optics," Adv. Photonics **2**(06), 066005 (2020).

33. R. Kingslake and R. Barry Johnson, "Chapter 5 - chromatic aberration," in *Lens Design Fundamentals (Second Edition)*, R. Kingslake and R. Barry Johnson, eds. (Academic Press, Boston, 2010), pp. 137–171, 2 edition ed.

34. "Dokument 8.1.2 - piezoceramic masses - data sheet englisch v2.00.0004," https://www.piezoproducts.com/wp-content/uploads/2020/03/JM_Piezo_Products-Data-Sheet-Piezoceramic-Masses-v2.00.0004.pdf. (Accessed on 09/28/2021).

35. "schott-d-263-t-eco-thin-glass-may-2013-eng.pdf," https://www.schott.com/d/advanced_optics/ea165ca6-b4f8-49ee-b989-072ddb2d2e4d/1.0/schott-d-263-t-eco-thin-glass-may-2013-eng.pdf. (Accessed on 09/28/2021).

36. "Clear flex 50 product information | smooth-on, inc.," https://www.smooth-on.com/products/clear-flex-50/. (Accessed on 09/28/2021).

37. P. Hartmann, R. Jedamzik, S. Reichel, and B. Schreder, "Optical glass and glass ceramic historical aspects and recent developments: a schott view," Appl. Opt. **49**(16), D157–D176 (2010).

38. "Thorlabs - ac254-250-a f = 250 mm, Ø1″ achromatic doublet, arc: 400 - 700 nm," https://www.thorlabs.de/thorproduct.cfm?partnumber=AC254-250-A. (Accessed on 09/15/2022).